Drop Size Distribution Retrieval Using ~~Dual Frequency Polarimetric Weather Radars~~Dual-Polarization Radar Observations at C-Band and S-Band

Daniel Durbin[1], Yadong Wang[1], and Pao-Liang Chang[2]

[1]Electrical and Computer Engineering Department, Southern Illinois University Edwardsville, Illinois, USA
[2]Central Weather Bureau, Taipei, Taiwan

Correspondence: Daniel Durbin (ddurbin@siue.edu)

Abstract. Having knowledge of the drop size distribution (DSD) is of particular interest to researchers as it is widely applied to quantitative precipitation estimation (QPE) methods. Polarimetric radar measurements have previously been utilized to derive DSD curve characteristics frequently modeled as a gamma distribution. Likewise, approaches using dual frequency measurements have shown positive results. Both cases have relied on the need to constrain the relationship between the DSD

5   parameters based on ~~prior knowledge or assumptions of the collected data~~location or assumed weather conditions. This paper presents a methodology for retrieving the DSD parameters using the dual frequency and polarimetric nature of measurements from a unique data set taken at co-located S-band and C-band dual polarization radars. Using the reflectivity and differential phase measurements from each radar, an optimization routine employing particle swarm optimization (PSO) and T-Matrix computation of radar parameters is able to accurately retrieve the gamma distribution parameters without the constraints re-

10   quired in previous methods. Retrieved results are compared to known truth data collected using a network of OTT PARSIVEL disdrometers in Taiwan in order to assess the success of this procedure.

1 Introduction

Knowledge of the Drop Size Distribution (DSD) for a given location is an incredibly valuable piece of information. The most ~~accurate~~ precise rainfall estimates can be achieved with an accurate assessment of the DSD. The applicability of deducing

15   localized DSDs to Quantitative Precipitation Estimation (QPE) is evident. QPE provides society with many benefits. Being able to precisely identify or even forecast heavy precipitation can help emergency and water management services better deploy their services and can alert others of dangerous flash floods, which can ultimately save lives. ~~The Drop Size Distribution (DSD)~~

     The DSD provides critical information about the composition of a given volume of atmosphere in a region of interest. It

20   is expressed as the number of particles for each drop size given as an equivalent sphere with a reference diameter, typically measured in millimeters. By knowing the DSD, important measures such as reflectivity (Z), rainfall rate, and total water content can be derived. These parameters are only as accurate as the DSD representation, which highlights the value of flexibility in the model.

The Marshall-Palmer distribution is a ~~widely used~~ well-known model for describing the DSD of rain (Marshall and Palmer, 1948)

25 . It is based on an exponential distribution and assumes that the DSD is spatially and temporally homogeneous. The intercept parameter of the Marshall-Palmer distribution, which is set to 8000, determines the overall scale of the distribution.

However, research has shown that the Marshall-Palmer distribution is limited in its applicability to different types of precipitation and atmospheric conditions. Specifically, it has been found that the Marshall-Palmer distribution is only accurate in the stratiform precipitative region~~(Marshall and Palmer, 1948)~~, which is a region of moderate, steady rainfall. As the rainfall rate

30 increases and diverges from this mode of precipitation, the intercept factor exhibits a large degree of variability (Sauvageot and Lacaux, 1995). While it can be a useful approximation, it has limiations that should be taken into account when using it in applications such as QPE.

A larger number of DSDs can be expressed generically in the form of a gamma function given by Equation 1 ~~(Ulbrich, 1983)~~ ~~.~~

35 $N(D) = N_0 D^{\mu} \exp(-\Lambda D)$

where $N(D)$ (m^{-3} mm^{-1}) is the concentration for each diameter D (mm), and μ (unitless), Λ (mm^{-1}), and N_0 are the shaping parameter, the exponential slope parameter, and the initial concentration of the distribution, respectively ~~.~~ (Ulbrich, 1983).

$$N(D) = N_0 D^{\mu} \exp(-\Lambda D) \tag{1}$$

While the gamma DSD provides more flexibility than the exponential or Marshall-Palmer distribution, its complexity can

40 make it difficult to use for retrieval purposes, as three unknown parameters must be solved, and the model is still limited in its ability to account for the smallest drop sizes. In the past, researchers have attempted to simplify the process by assuming a relationship between these parameters.

Extensive research has been conducted to ~~remotely estimate the drop size distribution (DSD)~~estimate DSDs, with many studies utilizing measurements taken at two frequencies. This is because using data from a single frequency is typically in-

45 sufficient for accurately estimating the DSD and can only provide information about a single parameter at a specific location ~~. (Meneghini et al., 1997). Gogucci and Baldini~~ (Meneghini et al., 1997). Gorgucci and Baldini (2016) demonstrated this approach using Global Precipitation Measurement (GPM) dual wavelength radar measurements. The surface reference technique is used to calculate path-integrated attenuation for each frequency so that a set of reflectivity and attenuation integral equations is formed. The system can then be solved for the DSD parameters that best match the measurements. The disadvantage

50 of the approach is that it relies on assuming μ is a function of the median volume diameter ~~. (Gorgucci and Baldini, 2016)~~ (Gorgucci and Baldini, 2016).

Williams et al. (2014) also worked to show dual wavelength approaches could be performed with GPM data. The underconstrainment issue was overcome by creating a distribution of standard deviations of the mean drop diameter using a large number of surface disdrometer measurements. Superior results were achieved relative to approaches that assume μ is a constant

55 in order to overcome the ill-constrained nature of the retrieval ~~.~~ (Williams et al., 2014). Many others have shown dual frequency measurements are exploitable for discerning these properties (e.g., Mardiana et al., 2004; Chandrasekar et al., 2005; Eccles, 1979; Kozu et al., 1991; Kummerow et al., 1989; Marzoug and Amayenc, 1994; Meneghini et al., 1992).

~~Attempts at retrieving DSD parameters utilizating dual polarization measurements~~ In addition to leveraging the scattering variances across different frequencies, there have also been ~~made.~~ efforts to retrieve DSD parameters using dual-polarization measurements. These efforts capitalize on the characteristic oblateness of raindrops which would obviously not be available in the case of the previously mentioned vertical profiles measured by GPM. Brandes et al. used S-band measurements of reflectivity and differential reflectivity to seek the gamma parameters (Brandes et al., 2002). An empirical relation is assumed between μ and Λ. While this relationship was applicable to both convective and stratiform rains, it was localized to the Florida region of the United States which was used for study. Similar approaches using horizontal and differential reflectivity have also been successful in experiments in Central Oklahoma but still rely on constrained relationships of the parameters (Cao et al., 2010).

The aim of this work is to solve for the three variables of the gamma drop size ~~distribution (DSD) without the need for additional constraints~~DSD. To achieve this, measurements taken at two frequencies with both vertical and horizontal polarizations are incorporated into optimization routines. This approach allows for the determination of DSD solutions that accurately represent the input reflectivity and specific differential phase information.

This paper is organized in the following manner. Section 2 conveys the methodology of this work. High-level design characteristics of the instruments used for data collection are provided, including the disdrometers and the two ground radars. Key elements of the data preprocessing routines are provided. ~~Although details of the T-matrix method are beyond the scope of this paper, its use in conjunction with Ryzhhov's model is explained, including significant assumptions. The optimization approach is explained and compared to other possible strategies.~~

~~The results are demonstrated through several~~ Prior to concluding thoughts in Section 4, Section 3 demonstrates the results through multiple examples, comparing the disdrometer collected DSDs with the retrieved results from the proposed algorithm ~~. In addition,~~ and an evaluation of the error when applied to QPE. A noteable increase in accuracy is found when estimating the rainfall rate using this proposed algorithm when compared to the traditional *Z-R* derived rainfall rate. Furthermore, we discuss and demonstrate a supplementary validation approach~~is discussed and demonstrated using the~~, utilizing C-band reflectivity data ~~that was not included in~~ previously excluded from the proposed optimization routines. This approach serves as an external validation mechanism for the proposed algorithm and provides a comparison of the results obtained from the algorithm with those obtained from the C-band reflectivity data. The results demonstrate the effectiveness of the proposed algorithm in retrieving accurate DSDs and its potential usefulness in radar systems that utilize more than one frequency.

2 Methods

2.1 Instrumentation

In the current work, the measurements of two co-located polarimetric radars, RCWF (S-band) and RCMD (C-band), are used in the algorithm development and validation. A photo of these two radars is shown in Figure 1, where RCWF and RCMD are located on the right and left panel, respectively. The Central Weather Bureau of Taiwan operates these two radars that provide real-time observations used for severe weather surveillance, quantitative precipitation estimation, hydrometeor classification,

and precipitation microphysics studies. These radars play a critical role in monitoring and forecasting precipitation in Taiwan and provide key data that ~~is~~ are useful in the research of preciptiative processes. The manufacturer models of RCWF and RCMD are the Weather Surveillance Radar 1988 Doppler (WSR-88D) and Gematronik, respectively. More technical specifications about these two radars can be found in Table 1. As shown in Figure 1, these two radars are adjacent to each other, and the

95 distance between them is much less than the range resolution (250 m). Since these two radars have the same polarization and location, the divergence of the observed differential phase (Φ_{DP}) and ~~reflectivity (Z)~~ Z can therefore be attributable to only radar frequency difference. These measurement differences are the key variables implemented in the retrieval method.

To validate the performance of the proposed algorithm, DSD data collected by a laser-based optical system, the OTT Particle Size Velocity (PARSIVEL or Parsivel) Disdrometer, is used as the ground truth. The Prasivel disdrometer derives the DSD

100 through the measured particle's size and velocity. There are 32 diameter and velocity bins available to measure particles with size between 0.062 mm to 24.5 mm and with velocity between 0.05 m s^{-1} to 20.8 m s^{-1}. The accuracy of Parsivel Disdrometer has been studied by Sheppard (2007); Jaffrain and Berne (2011).

Sampling with the OTT Parsivel may exhibit some degree of statistical variance, which is a common characteristic of all measurements. Microphysical events are inherently stochastic in nature and the physical sampling effects and noise also play

105 roles in the deviations (Sheppard, 2007). The Parsivel used in this dataset has been compared to more accurate 2D disdrometer data in order to gauge the variance. The findings of Jaffrain et al. (2011) demonstrated that sampling uncertainty is minimal for small to moderate drop sizes ~~, but it~~ but starts to escalate for larger classes (greater than 2.0 mm). Notably, the data set used in this study lacks a large representation of drop sizes exceeding 2 mm, which is advantageous as the smaller class measurements can be assumed to be more accurate(Jaffrain and Berne, 2011).

110 Possible error sources of OTT Parsivel were investigated by Angulo-Martínez et al. (2018). It was found that uneven power distribution over the beamwidth or any time variation can adversely ~~effect~~ affect the accuracy. Other factors, such ~~and~~ as the angle of the drop trajectory, coincidentally observed particles, and particles that intersect with only the edge will also lead to biases.

The locations of two dual polarization radars and OTT Parsivel disdrometers are depicted in Figure 2 with stars and circles,

115 respectively. The complex terrain of Taiwan presents a ~~significant~~ challenge due to ~~frequent~~ radar beam blockage. The Central Mountain Range (CMR) is visible in Figure 2, running from the north to the south of the island, with the highest peak exceeding 3800 m. To mitigate the effects of vertical variability in radar measurements, only data from the two lowest unblocked tilts ~~were~~ are used in the DSD retrieval. Additionally, two rings with ranges of 20 km and 70 km are shown in Figure 2. The performance of the proposed approach was validated only ~~with~~ using the disdrometers located within these two ranges. More details related

120 to the validation data selection will be provided in the following section.

The final sources of error we attempted to mitigate relate to the radar measurement itself. Observation bias is a primary concern, stemming from the inherent differences between radar and disdrometer measurements-where radars capture data over a large volume and disdrometers provide point-specific observations leading to potential discrepancies in data interpretation. Additionally, vertical variations in drop size DSDs pose a significant challenge due to the radar's observation points being

125 several hundred meters above the ground. This discrepancy is particularly problematic for all radar-based DSD retrieval

methods. The various equipment heights and locations are shown in Table 2. To address this, we constrained our analysis to data from the two lowest elevation tilts of radar scans. Although it does not fully eliminate the issue, this approach helps to reduce the impact of this error source. These aspects underscore the complexities involved in accurately retrieving DSDs and highlight the necessity of carefully considering these factors when analyzing radar and disdrometer data.

130 ## 2.2 Radar and Disdrometer Data

2.2.1 Preprocessing of Radar and Disdrometer Data

The Z and Φ_{DP} fields from both C- and S-band radars are the proposed parameters for DSD retrieval, and the qualities of both fields ~~were~~ are examined and processed through a set of quality control procedures. The quality control process pertaining to the reflectivity field includes identifying and removing nonprecipitation radar echoes and smoothing along the radial direction.

135 Any ~~gate~~ gates associated with correlation coefficient (ρ_{HV}) less than 0.98 ~~was considered as likely~~ are considered as possibly produced by nonprecipitative clutter, and reflectivity is excluded from the average operation. The obtained reflectivity is then smoothed with a 4 km smoothing window along each radial direction. The raw Φ_{DP} field of RCMD ~~was~~ is processed with the new Selex-Gematronik family of digital receiver and signal processor (GDRX) (Bringi et al., 2005). The GDRX processes the raw field using the field unwrapping, "good data" mask application, and finite impulse response (FIR) filtering. The details of

140 the procedure can be found in Bringi et al. (2005). The similar procedure is also applied on the raw Φ_{DP} field from RCWF. Examples of processed reflectivity and differential phase fields are shown in Figure 3, where panels "a" ("c") and "b" ("d") show the reflectivity (raw differential phase) measured by S-band and C-band, respectively. The yellow arrow in panel "a" indicates the radial path from the radars to the disdrometer location of interest. It should be noted the reflectivity fields from both frequencies ~~show a similar trend~~ are consistent, and the difference is mainly caused by the attenuation. The differential

145 phase fields, on the other hand, show significant difference, which indicates that the differential phase is more sensitive to the radar frequency. A detailed analysis of the impact from frequency on the differential phase and specific differential phase is presented in Section 3.1.

The DSD parameters are derived from the Parsivel disdrometer observations through the approach proposed by Raupach and Berne (Raupach and Berne, 2015). In this approach, ~~information about~~ data concerning individual raindrops, including

150 their diameters, fall velocities, and the effective sampling areas of the instrument ~~was~~ are recorded. The drops are binned into diameter classes, and the concentration is then calculated ~~through~~

$$N_i = \frac{1}{\Delta D_i \Delta t} \sum_{j=1}^{M} \frac{1}{S_j V_j}$$

using Equation 2 where N_i is the drop concentration for the ith equivolume diameter class, S is the effective sampling area, V is the particles velocity, and ΔD_i and Δt are the class width and sampling period, respectively.

155 $$N_i = \frac{1}{\Delta D_i \Delta t} \sum_{j=1}^{M} \frac{1}{S_j V_j} \tag{2}$$

2.2.2 Data selection

The algorithm development and validation ~~for RCWF and RCMD~~ were based on ~~nine~~ ten days of data collected by RCMD and RCWF. These days included June 1, 2017, June ~~11-16~~11-17, 2017, January 7, 2018, and May 7, ~~2018, during which~~ 2018. The majority of these days correspond to the Meiyu season in Taiwan and represent events of light to moderate precipitation ~~was~~ which were observed in the region covered by the two radars. These days provided data representative of multiple precipitation intensities.

One challenge in using both RCWF and RCMD is that they operate under different volume coverage patterns (VCPs). As a result, there is a slight time lag between scans from these two radars when observing the same location. To minimize the retrieval biases caused by the DSD variation during the time lag, the time stamp differences between scans from the two radars were limited to within one minute. This time limitation helped ensure that the ~~retrieved DSD was as accurate as possible, given the time lag between the two radars.~~ radar data adhere to an acceptable degree of synchronization.

In this work, the differences in both reflectivity and differential phase fields obtained from the S-band and C-band radars play critical roles in the DSD retrieval. ~~The use of both S-band and C-band radars is necessary because the differing wavelengths allow for more accurate estimation of the DSD. The differences between the reflectivity and differential phase fields from both radars provide important information about the size distribution of the hydrometeors.~~

~~It is important to note that sufficient differences~~ Sufficient differences are expected from the two frequencies, ~~specifically differential phase, in order to accurately estimate the DSD~~primarily differential phase. If the differences are too small, ~~it~~ the algorithm may result in a biased or inaccurate retrieval of the DSD. Thus, it is crucial to carefully select the observation range ~~and ensure that there are sufficient differences in the fields to obtain an accurate DSD estimation.~~ such that enough differential phase difference has been experienced by the radar return.

Another important factor to consider is that biases in the retrieved DSD can accumulate along the range. This means that the farther the distance between the radar and the target area, the larger the error in the retrieved DSD. This ~~range~~ attenuation effect is a predictable issue in radar data processing, and it underscores the importance of carefully selecting the range of interest when estimating the DSD.

To achieve reasonable results, the following criteria for candidate data ~~was~~ are therefore used:

- ~~Range > 25 km and Range < 100~~ 25 km < Range < 70 km

- $Z^S > 25$ ~~dB~~ dBZ

This set of criteria is designed to strike a balance between creating sufficient deviation between C and ~~S band~~ S-band differential phases for an accurate DSD retrieval, while also preventing excessive error accumulation. Additionally, a reflectivity threshold of 25 ~~dB~~ dBZ is imposed to ensure that there is enough observable precipitation in the terminal gate where the disdrometer is located.

Figure 3 illustrates an example of the raw Z data captured by the S-band and C-band radars with the location of the disdrometers indicated using black circles. Panels "a" and "b" show the reflectivity data obtained by the S-band and C-band radars,

respectively. The yellow arrow in panel "a" indicates the radial path extending from the radars to the location of interest, where the disdrometer is also located, and the DSD along this radial is retrieved. Panels "c" and "d" display the raw Φ_{DP} fields gathered by the S-band and C-band radars ~~. The Φ_{DP} information is critical to accurately retrieve the drop size distribution in the study as it~~ which serves as the primary source of independent inputs to the algorithm. This figure serves as a visual representation of the data used in the DSD retrieval algorithm and demonstrates the differences in the data between the S-band and C-band radars. Figure 4 shows the post-processed Z (panel "a") and Φ_{DP} (panel "b") fields along the yellow arrow of Figure 3. The measurements from S- and C-band radar are shown with blue and red color, respectively.

2.3   Drop Size Distribution With an Artificial Intelligence Method

The flowchart of the proposed DSD retrieval algorithm is presented in Figure 5. Three variables of S-band reflectivity $(Z^S(r,\theta))$ ~~,~~ and differential phase from both S- and C-band $(\phi_{DP}^S(r,\theta), \phi_{DP}^S(r,\theta))$ are implemented as inputs, where r and θ are the coordinate of range and azimuthal angle, respectively. The analysis exclusively ~~employed~~ employs S-band reflectivity as it ~~was~~ is considered a more dependable variable than Z^C in the dataset. The exclusion of Z^C ~~was~~ is prompted by the potential to introduce more inaccuracies into the procedure due to the radar's heightened vulnerability to attenuation and uncertainty in calibration precision. Since Z^C displays high correlation with Z^S, it is unlikely that the inclusion of C-band reflectivity would furnish any additional useful insights into the retrieval. Moreover, the exclusion of Z^C from the process serves as an additional validation parameter, as discussed further in Section 3.

The radar variables from a given gate are first preprocessed with the routine described in Section 2.2.1, and the processed data are then used to retrieve three parameters as described in Section 2.3.2.

2.3.1   T-Matrix Computation of Radar Parameters

In the retrieval procedure, a set of DSD parameters in Equation 1 ~~are~~ is first initialized within commonly observed ranges of the parameters (Zhang et al., 2001):

- $10^2 < N_0 < 10^{10}$

- ~~$-2 < \mu < 10$~~ $0 < \mu < 10$

- $0 < \Lambda < 15$

With the initial parameters, the DSD $(N(D))$ is calculated, and radar variables of Z^S, K_{DP}^S (K_{DP}^C) and specific attenuation (A) are then calculated with the following equations integrated from 0 to a maximum diameter (D_{max}) of 8 mm (Ryzhkov et al., 2013):

$$Z = \frac{4\lambda^4}{\pi^4 |K_w|^2} \int_0^{\infty \, D_{max}} \left| f_{\underline{a}\underline{b}}^{\underline{\pi}}(\underline{\pi} D) \right|^2 N(D)dD \tag{3}$$

$$K_{DP} = \frac{0.18\lambda}{\pi} \int_0^{\infty \, D_{max}} \mathrm{Re}\{ f_{\underline{a}}(\underline{0})_{\underline{b}}^{\underline{0}}(\underline{D}) - f_{\underline{b}}(\underline{0})_{\underline{a}}^{\underline{0}}(\underline{D}) \} N(D)dD \tag{4}$$

220

$$A = 8.686 \times 10^{-3}\lambda \int_0^{\infty \, D_{max}} \mathrm{Im}\{ f_{\underline{b}}(\underline{0})_{\underline{b}}^{\underline{0}}(\underline{D}) \} N(D)dD \tag{5}$$

In ~~the above equations, backscattering amplitudes, $f_a(0)$ $(f_a(\pi))$ and $f_b(0)$ $(f_b(\pi))$, at horizontal and vertical polarizations were~~ these equations, vertical polarization scattering amplitudes, $f_a^0(D)$ $(f_a^\pi(D))$, and horizontal polarization scattering amplitudes, $f_b^0(D)$ $(f_b^\pi(D))$, are calculated with the T-Matrix method (Waterman, 1965), where 0 and π indicate forward and backward ~~scattering amplitude, respectively. The canting angle corresponding to the calculated amplitudes was zero, and the~~ directions respectively. These formulations make use of a simplification with zero canting angle which will introduce only a small error due to the limitation of elevation tilts. The dielectric constant of water ~~was~~ is referenced at 10 degrees Celsius ~~.~~ which is a reasonable temperature for the radar volume situated between the melting layer and the ground level temperature of Taiwan during these dates.

With the obtained K_{DP} field, the Φ_{DP} field from both the S- and C-band ~~radar~~ radars were then calculated through Equation 6, where ΔR represents the range difference between the ith gate and the previous gate.

$$\Phi_{DP}(r_i, \theta) = K_{DP}\Delta R + \Phi_{DP}(r_{i-1}, \theta) + \Phi_{DP}^{sys}$$

~~where~~ Φ_{DP}^{sys} is the ~~minimum~~ system Φ_{DP} ~~, and Φ_{DP}^{sys} for both radars could be found from Table 1.~~ be found in Table 1 for both radars.

$$\Phi_{DP}(r_i, \theta) = 2K_{DP}\Delta R + \Phi_{DP}(r_{i-1}, \theta) + \Phi_{DP}^{sys} \tag{6}$$

2.3.2 Optimization Routine

The estimation of radar variables can be achieved by adjusting ~~the DSD parameters~~ a parameterized DSD in order to reduce the difference between the estimated and observed values. As this difference decreases, the optimization problem gradually approaches a minimum value, ultimately resulting in the retrieval of the desired information. Essentially, the retrieval problem can be considered as an optimization problem where the goal is to find the optimal set of parameters that minimize the difference between the estimated and observed values.

Multiple methods exist for minimizing the error between the simulated radar variables and the measured variables. A relatively simple approach that was first used is the Gauss-Newton method. While it can quickly converge ~~on~~ to a solution, the

technique will often only find local minima rather than the global minimum of the solution space. Another early attempt used the genetic algorithm (GA), which very reliably found better solutions. The GA, however, was very computationally intensive and relied on fine-tuning of the crossover and mutation factors to efficiently solve for the DSD.

Particle Swarm Optimization (PSO) was ultimately used for this work since it is comparatively more efficient at seeking the most representative DSD. Figure 6 shows the organization of the PSO application. For a gate with preprocessed reflectivity and differential phase measurements, particles with random N_0, μ, and Λ are initialized. Ranges for the particle positions ~~were~~ are chosen according to commonly observed intervals (Zhang et al., 2001). In this manner, a coordinate space is created in which each DSD parameter is a dimension.

The three coordinates of each particle position collectively define a DSD that is used to calculate Z^S and $\Phi_{DP}^{S,C}$. Various cost functions which measure the distance from the preprocessed truth data were tried. The fitness function given by Equation 7 allows for relative weightings to be applied to each variable. Experimentally determined values ($\alpha = 5$, $\beta = \gamma = 1$) led to reliable retrievals. It should also be noted that Z^S is expressed as a logarithmic value rather than in linear units.

$$\text{Cost} = \alpha \left| \frac{Z_{\text{simulated}}^S - Z_{\text{measured}}^S}{Z_{\text{measured}}^S} \right| + \beta \left| \frac{\Phi_{DP,\text{ simulated}}^S - \Phi_{DP,\text{ measured}}^S}{\Phi_{DP,\text{ measured}}^S} \right| + \gamma \left| \frac{\Phi_{DP,\text{ simulated}}^C - \Phi_{DP,\text{ measured}}^C}{\Phi_{DP,\text{ measured}}^C} \right| \tag{7}$$

The cost of every particle is calculated, and the iteration's current best solution as well as the global best solution of all iterations are recorded. The particle positions are then updated according to Equation 8 where ~~α~~ ϵ is the local acceleration factor, ~~β~~ ζ is the global acceleration factor, ~~and~~ r_1 and r_2 are random numbers between zero and one that are generated for each particle, and i denotes the current iteration. This allows the particles to move towards the current and global best solutions and possibly find better solutions along the path. The convergence speed must be weighed against the possibility of "overshooting" viable candidate solutions. ~~α and β~~ ϵ and ζ were determined experimentally, and values of 0.15 and 0.0015 were used for processing the overall data set.

$$\begin{bmatrix} N_0 \\ \mu \\ \Lambda \end{bmatrix}_{i+1} = \begin{bmatrix} N_0 \\ \mu \\ \Lambda \end{bmatrix}_{i} + \underline{\alpha}\epsilon \left\{ \begin{bmatrix} N_0 \\ \mu \\ \Lambda \end{bmatrix}_{\substack{\text{iteration} \\ \text{best}}} - \begin{bmatrix} N_0 \\ \mu \\ \Lambda \end{bmatrix}_{i} \right\} r_1 + \underline{\beta}\zeta \left\{ \begin{bmatrix} N_0 \\ \mu \\ \Lambda \end{bmatrix}_{\substack{\text{global} \\ \text{best}}} - \begin{bmatrix} N_0 \\ \mu \\ \Lambda \end{bmatrix}_{i} \right\} r_2 \tag{8}$$

The swarm ~~consisted~~ consists of five thousand particles which ~~were~~ are allowed four hundred iterations for each retrieval. A stability or minimum error criteria could easily be implemented to halt the retrieval that is displayed in Figure 6.

2.3.3   Retrieval Along Radial

The ultimate goal of the retrieval process is to obtain the DSD ~~for the specific disdrometer location~~ that is similar to that of the disdrometer measurement. To accomplish this, the PSO retrieval algorithm is applied to each ~~location~~ gate, starting from the one nearest the radar. The input reflectivity of the final gate must take into account any attenuation experienced between

270 the radar and the disdrometer gate. Once a representative DSD is obtained for a gate, the attenuation is calculated, and the reflectivity for the next farthest gate is adjusted accordingly. This iterative process, as shown in Figure 7, continues at 4 km intervals until the retrieval is performed at the terminal gate at the disdrometer location. ~~This process is illustrated in Figure 7.~~

By iteratively refining the DSD retrieval and adjusting the reflectivity for each gate, the algorithm effectively accounts for the changes in reflectivity due to attenuation along the path and provides an accurate representation of the DSD at the specific

275 disdrometer location. Specifically, the radial-based approach used in this study involves starting with the first gate from each radial, which is assumed to be unattenuated. The measured reflectivity and differential phase are then directly input into the PSO algorithm to obtain the optimized DSD for this gate. For the next gate, the attenuation is calculated using the DSD from the previous gate and accounted for in the retrieval process. The true reflectivity for each gate is the measured reflectivity plus the attenuation calculated using the previously retrieved DSD. This process continues until the gate with the disdrometer is

280 reached, at which point the final retrieval is performed.

3   Performance Evaluation

The ~~current study did not conduct a rigorous statistical analysis due to the limitations of the data, including the requirement for tightly synchronized observations from the radar. Instead, the primary aim was to demonstrate proof of concept and prototype the methodology for future studies that would incorporate a more systematic statistical analysis. While the results of~~ evaluation

285 of the proposed algorithm was carried out through both qualitative and quantitative methods. Initially, the ~~current study are promising, further work is needed to evaluate the accuracy and robustness of the proposed approach. A more comprehensive statistical analysis could be performed in the future to further validate the method and identify any potential sources of error. Nine days of data~~ retrieved DSDs were subjectively compared to the DSDs measured by the disdrometers at the times nearest to the radar scans. This qualitative comparison provides a preliminary measure of the algorithm's overall accuracy

290 as adjustments were made to its parameters. A subsequent discussion of the role of using two frequencies rather than a single frequency approach highlights the value of using the C-band reflectivity (unused in the retrieval) for further validation of the along-radial results. Following the fine-tuning of the cost function and PSO parameters, a more rigorous quantitative analysis was performed. This involved calculating the rainfall rates based on the disdrometer-recorded DSDs, which were considered as the benchmark, and comparing these rates to those obtained from the retrieved DSDs. Additionally, the calculated rainfall rates

295 were contrasted with those derived using the traditional *Z*-*R* relationship methodology, offering a comprehensive evaluation of the algorithm's performance.

For the performance validation of this study, data spanning ten days from 2017 and 2018 ~~is used in the performance validation in the current work~~ were utilized. The stringent criteria for time synchronization narrowed the dataset to 167 cases that not only met the synchronization requirements but also had the requisite data quality and fell within the disdrometer range requirement.

300 ~~Therefore, the performance of the proposed approach is validated through qualitatively comparing the DSD obtained from the proposed approach and calculated from the~~

3.1 Qualitative Assessment

Figure 8 showcases a representative selection of the retrieved DSDs the algorithm generated as compared to the disdrometer data. Cases were systematically sampled across the dataset's collection period to accurately reflect the algorithm's retrieval performance. These cases strictly adhere to the time synchronization criteria established by our data quality standards and exhibit reflectivity values at the terminal gate that exceed the minimum threshold. The radar scan time tags are specified with precision down to the second, whereas disdrometer measurements are recorded on a per-minute basis. Consequently, both the preceding and subsequent disdrometer timestamps are presented (red and green, respectively), as well as the closest time (blue). This approach acknowledges instances where these adjacent timestamps may more accurately represent the radar data.

The majority of cases show a high degree of agreement across the spectrum of drop sizes, with particularly strong correlation observed for the measurements of larger drop sizes. It can be found from Figure 8 that the retrieved DSD fits the disdromter observations very well for larger drops ($D > 0.5$ mm). Deviations can be found in cases such as 20170613 - 08:04:49 and 20180107 - 09:26:32 for smaller drops ($D < 0.5$ mm).

Not all disdrometer sizes need to be equally prioritized for accurate fitting. Examination of Equations 3 and 4 reveals that the contribution to radar parameters from each diameter increases with the size of the drop. Furthermore, previous research evaluating the accuracy of disdrometers across various drop sizes indicated that drops of 0.6 mm and larger are the first reliably measured sizes by optical disdrometers (Tokay et al., 2001). This finding supports the notion that inaccuracies in measuring smaller drop sizes do not significantly impact the calculations of reflectivity or DSD-derived metrics such as rain rate and attenuation. While some researchers have proposed that the goal of a retrieval should be to fit the predominance of the size spectrum (Adirosi et al., 2013), it is clearly more important to represent medium to large diameters when the integrated parameters are the focus.

The role of the additional frequency in providing extra information is a key question addressed in this study. The viability of employing dual-polarization measurements at C-band and S-band for rainfall estimation can be demonstrated through a simple simulation presented in this section. This simulation involves calculating the backward and forward scattering amplitudes for

selected drop sizes through the T-Matrix method, followed by deriving the specific differential phase (K_{DP}) values for varying drop size distributions using a gamma-modeled DSD, analyzing a diverse range of μ and Λ values, while keeping N_0 fixed at 8000, as depicted in Figure 9. The simulation results highlight that K_{DP} values exhibit distinct separations at the two wavelengths (10.0 cm for S-band and 5.0 cm for C-band) particularly for Λ values of 2 and 4. Furthermore, it is observed that with larger Λ values, the differentiation between the two frequencies becomes less pronounced, as can be inferred from such quickly collapsing distributions. This simulation underscores the potential of using dual-polarization measurements at C and S radar bands for DSD retrieval.

To investigate this, the retrieval algorithm was applied to select cases with the contribution of the C-band reflectivity excluded from the analysis. This exclusion was achieved through modification of the cost function in Equation 9 ($\alpha = 5$ and $\beta = 1$ were again chosen). The aim was to determine if both frequency bands were necessary to obtain accurate retrievals of the DSD.

$$\text{Cost} = \alpha \left| \frac{Z^S_{\text{simulated}} - Z^S_{\text{measured}}}{Z^S_{\text{measured}}} \right| + \beta \left| \frac{\Phi^S_{DP,\,\text{simulated}} - \Phi^S_{DP,\,\text{measured}}}{\Phi^S_{DP,\,\text{measured}}} \right| \tag{9}$$

Figure 10 shows the results of the algorithm applied with Equation 9 to the same scenario as the first case in Figure 8. The terminal gate reflectivity factor is 40.0 dBZ with K_{DP} equal to 0.84 and 1.15 at S and C-bands, respectively. Using two radar bands clearly increases the accuracy of the fit in this example. It is highly unlikely using a single frequency could produce comparably favorable results since no examples of DSD retrieval techniques using one wavelength were found in the literature which did not rely on a $\mu - \Lambda$ relationship or other constraint. Therefore, an exhaustive comparison of the performance between the dual frequency and S-band only cases was not conducted, but several of these spot checks such as shown in Figure 10 were produced.

To ensure the accuracy of the retrieval algorithm, one can utilize the C-band parameters obtained from the retrieved DSDs to validate the S-band parameters. To accomplish this, the attenuation that is calculated from the retrieved DSDs can be applied to correct the C-band reflectivities affected by the large attenuation experienced over the path. ~~However, the phase of the C-band return is less susceptible to attenuation and can be used as a useful tool for validating the retrieval algorithm.~~

Figure 11 suggests that the S-band reflectivity is ~~relatively unaffected~~ less affected by attenuation as expected. The blue ~~circles~~ dashed line in the plot represent the raw reflectivity values measured by the S-band radar, which ~~demonstrate~~ demonstrates the relatively low attenuation at this wavelength. The blue ~~triangles~~ solid line in the plot ~~represent~~ represents the attenuation-corrected reflectivity values measured by the S-band radar.

The corrected C-band reflectivities are shown ~~with red triangles~~ as the solid red line in the plot and are seen to match well with the S-band values. This indicates that the ~~correction~~ attenuation factor derived from the retrieved DSD is effective in converting the C-band reflectivities to equivalent S-band values. By using this correction factor, we can confirm that the retrieved DSD accurately predicts the atmospheric effects at both radar bands.

3.2 Quantitative Assessment

A comprehensive quantitative analysis was conducted on the 167 cases, utilizing the disdrometers in Table 2, with a particular focus on the algorithm's accuracy in QPE, where the importance of accuracy is most prominently showcased. Rainfall rates were calculated using the retrieved DSDs according to Equation 10 with $v(D)$ given by Equation 11 where D is given in mm and $v(D)$ is in mm/s (Ulbrich, 1983). For comparison, the S-band reflectivity data was applied using the WSR-88D *Z-R* relationship as outlined in Equation 12 (Ulbrich and Lee, 1999). The Parsivel data was used to calculate the ground truth via Equation 13 where D_j is the equivolume diameter of the jth recorded drop, S is the effective sampling area, and Δt is the sampling period Raupach and Berne (2015).

$$R = \frac{\pi}{6} \int_0^{D_{\max}} D^3 N(D) v(D) dD \tag{10}$$

$$v(D) = 9650 - 10300 \exp(-0.6D) \tag{11}$$

$$Z = 300 R^{1.4} \tag{12}$$

$$R_d = \frac{6\pi \times 10^4}{\Delta t} \sum_{j=1}^{M} \frac{D_j^3}{S_j^2} \tag{13}$$

The evaluation involved comparing the rainfall rates derived from the *Z-R* relationship and the retrieval algorithm against the ground truth values from the Parsivel disdrometer, whose biases were discussed in Section 2. This comparison was based on the Relative Absolute Error (RAE) as defined in Equation 14, where R_d represents the rainfall rate estimated from the disdrometer, and R denotes the rainfall rates from the methods being compared.

$$\text{RAE} = \frac{|R_d - R|}{R_d} \tag{14}$$

Figure 12 features a time series plot illustrating the RAE outcomes for both methodologies. The retrieval algorithm's accuracy is depicted by the blue line, while the *Z-R* relationship benchmark is shown in red. This visualization highlights that the proposed method of estimating rainfall rates using retrieved DSD parameters significantly enhances accuracy over the traditional *Z-R* relationship. Specifically, the median RAE for the *Z-R* method is 0.72, while the retrieval results correspond to a median of 0.53, marking a notable improvement of 26.4 % in this study's context.

It is important to acknowledge a notable limitation observed in the performance of the retrieval algorithm, as reflected in the results. Specifically, the algorithm has the potential to significantly overestimate the rainfall rate. Closer examination reveals

that such discrepancies arise from ill-posed conditions for retrieval. Although incorporating multiple frequencies enhances the capability to retrieve the DSD, the K_{DP} and reflectivity values must still exhibit a consistent correlation. Deviations from this correlation can mislead the algorithm, yielding suboptimal outcomes. Therefore, incorporating correlation criteria stands out as a promising direction for enhancing algorithmic accuracy in future research endeavors.

4 Conclusions

A novel approach to retrieving the DSD using PSO has been discussed. While the retrieval is unconstrained regarding the gamma distribution parameters, the price is the additional data needed. The authors feel that radar systems utilizing more than one frequency will continue to become more commonplace. The value of dual polarization in radars is already universally accepted. Algorithms such as the one prototyped in this work will become more valuable as radar systems produce data with this type of increased diversity.

There are several limitations in this research which have been briefly mentioned and which future work should address. ~~As stated, a statistical approach for evaluating the fitness of the DSDs and algorithm as a whole is needed. Excluding unreliable drop diameters may be a necessary step in any future rigorous evaluation methodology.~~

A larger dataset or alternative preprocessing criteria should be assessed for long-term evaluation of the approach. While ten days of data were screened, the selection process for useful cases was highly discriminatory. Only measurements from the two radars which were synchronized within ~~two minutes and identical in elevation angle~~ one minute became candidates. Of these, only data with corresponding disdrometer truth data and minimum terminal gate reflectivity were included in the processing pool. Preprocessing the measurements led to the greatest reduction in potential data. The majority of these cases were excluded because of data quality ~~, in most cases~~ primarily due to unreliable phase profiles. Future work should exhaustively assess the approach by processing a larger amount of high quality data.

One focus of this project was to show that N_0, μ, and Λ are independently solvable when incorporating both multi-frequency and multi-polarization information. Restricted relationships between the variables are still highly useful. If the intended ~~use~~ application of any retrieval algorithm can utilize a constraint with high confidence, the DSD retrieval process becomes much more efficient. The tradeoff is that shaping characteristics may not be captured, which is why study of more flexible retrieval processes should continue.

The optimization approach involves various adjustable parameters, including swarm size, number of iterations, and acceleration coefficients. Fine-tuning these parameters could result in faster and more optimal results. Moreover, adapting the algorithm to function as an embedded application for field testing is also a promising area for further development.

Code and data availability.

The datasets and source code used in this study are available from the corresponding ~~authors upon request(ddurbin@siue.edu or yadwang@siue.edu).~~ author upon request.

Author contributions.

Dr. Yadong Wang and Daniel Durbin ~~conceived the original idea of using~~ originated the initial concept of utilizing dual frequency, dual polarization measurements for DSD retrieval and ~~prototyped initial algorithms to show proof of concept~~developed preliminary algorithms to demonstrate its feasibility. Daniel Durbin further applied the PSO technique, processed the data set, and prepared the ~~draft~~ drafts of this paper. Both authors collaborated on the development of the final algorithm. Dr. P.-L. Chang provided and processed radar data from CWB and was further involved in algorithm discussion and article authoring.The Central Weather Bureau of Taiwan provided the unique data used in the project.

Competing interests.

The authors declare that there is no conflict of interest.

Acknowledgements. The authors thank the radar engineers at CWB for helping collect and process the radar data used in the study.

References

Adirosi, E., Baldini, L., Lombardo, F., Russo, F., and Napolitano, F.: Comparison of different fittings of experimental DSD, in: AIP Conference Proceedings, AIP, https://doi.org/10.1063/1.4825850, 2013.

Angulo-Martínez, M., Beguería, S., Latorre, B., and Fernández-Raga, M.: Comparison of precipitation measurements by OTT Parsivel[2] and Thies LPM optical disdrometers, Hydrology and Earth System Sciences, 22, 2811–2837, https://doi.org/10.5194/hess-22-2811-2018, 2018.

Brandes, E. A., Zhang, G., and Vivekanandan, J.: Experiments in Rainfall Estimation with a Polarimetric Radar in a Subtropical Environment, Journal of Applied Meteorology, 41, 674–685, https://doi.org/10.1175/1520-0450(2002)041<0674:eirewa>2.0.co;2, 2002.

Bringi, V. N., Thurai, M., and Hannesen, R.: Dual-Polarization weather radar handbook, 2nd ed. Neuss, p. 163 pp, 2005.

Cao, Q., Zhang, G., Brandes, E. A., and Schuur, T. J.: Polarimetric Radar Rain Estimation through Retrieval of Drop Size Distribution Using a Bayesian Approach, Journal of Applied Meteorology and Climatology, 49, 973–990, https://doi.org/10.1175/2009jamc2227.1, 2010.

Chandrasekar, V., Li, W., and Zafar, B.: Estimation of raindrop size distribution from spaceborne Radar observations, IEEE Transactions on Geoscience and Remote Sensing, 43, 1078–1086, https://doi.org/10.1109/tgrs.2005.846130, 2005.

Eccles, P. J.: Comparison of Remote Measurements by Single- and Dual-Wavelength Meteorological Radars, IEEE Transactions on Geoscience Electronics, 17, 205–218, https://doi.org/10.1109/tge.1979.294650, 1979.

Gorgucci, E. and Baldini, L.: A Self-Consistent Numerical Method for Microphysical Retrieval in Rain Using GPM Dual-Wavelength Radar, Journal of Atmospheric and Oceanic Technology, 33, 2205–2223, https://doi.org/10.1175/jtech-d-16-0020.1, 2016.

Jaffrain, J. and Berne, A.: Experimental Quantification of the Sampling Uncertainty Associated with Measurements from PARSIVEL Disdrometers, Journal of Hydrometeorology, 12, 352–370, https://doi.org/10.1175/2010jhm1244.1, 2011.

Kozu, T., Nakamura, K., Meneghini, R., and Boncyk, W.: Dual-parameter radar rainfall measurement from space: a test result from an aircraft experiment, IEEE Transactions on Geoscience and Remote Sensing, 29, 690–703, https://doi.org/10.1109/36.83983, 1991.

Kummerow, C., Mack, R. A., and Hakkarinen, I. M.: A Self-Consistency Approach to Improve Microwave Rainfall Rate Estimation from Space, Journal of Applied Meteorology, 28, 869–884, https://doi.org/10.1175/1520-0450(1989)028<0869:ascati>2.0.co;2, 1989.

Mardiana, R., Iguchi, T., and Takahashi, N.: A dual-frequency rain profiling method without the use of a surface reference technique, IEEE Transactions on Geoscience and Remote Sensing, 42, 2214–2225, https://doi.org/10.1109/tgrs.2004.834647, 2004.

Marshall, J. S. and Palmer, W. M. K.: THE DISTRIBUTION OF RAINDROPS WITH SIZE, Journal of Meteorology, 5, 165–166, https://doi.org/10.1175/1520-0469(1948)005<0165:tdorws>2.0.co;2, 1948.

Marzoug, M. and Amayenc, P.: A Class of Single- and Dual-Frequency Algorithms for Rain-Rate Profiling from a Spaceborne Radar. Pad I: Principle and Tests from Numerical Simulations, Journal of Atmospheric and Oceanic Technology, 11, 1480–1506, https://doi.org/10.1175/1520-0426(1994)011<1480:acosad>2.0.co;2, 1994.

Meneghini, R., Kozu, T., Kumagai, H., and Boncyk, W. C.: A Study of Rain Estimation Methods from Space Using Dual-Wavelength Radar Measurements at Near-Nadir Incidence over Ocean, Journal of Atmospheric and Oceanic Technology, 9, 364–382, https://doi.org/10.1175/1520-0426(1992)009<0364:asorem>2.0.co;2, 1992.

Meneghini, R., Kumagai, H., Wang, J., Iguchi, T., and Kozu, T.: Microphysical retrievals over stratiform rain using measurements from an airborne dual-wavelength radar-radiometer, IEEE Transactions on Geoscience and Remote Sensing, 35, 487–506, https://doi.org/10.1109/36.581956, 1997.

Raupach, T. H. and Berne, A.: Correction of raindrop size distributions measured by Parsivel disdrometers, using a two-dimensional video disdrometer as a reference, Atmospheric Measurement Techniques, 8, 343–365, https://doi.org/10.5194/amt-8-343-2015, 2015.

Ryzhkov, A. V., Kumjian, M. R., Ganson, S. M., and Khain, A. P.: Polarimetric Radar Characteristics of Melting Hail. Part I: The-
oretical Simulations Using Spectral Microphysical Modeling, Journal of Applied Meteorology and Climatology, 52, 2849–2870, https://doi.org/10.1175/jamc-d-13-073.1, 2013.

Sauvageot, H. and Lacaux, J.-P.: The Shape of Averaged Drop Size Distributions, Journal of the Atmospheric Sciences, 52, 1070–1083, https://doi.org/10.1175/1520-0469(1995)052<1070:tsoads>2.0.co;2, 1995.

Sheppard, B. E.: Sampling Errors in the Measurement of Rainfall Parameters Using the Precipitation Occurrence Sensor System (POSS),
Journal of Atmospheric and Oceanic Technology, 24, 125–140, https://doi.org/10.1175/jtech1956.1, 2007.

Tokay, A., Kruger, A., and Krajewski, W. F.: Comparison of Drop Size Distribution Measurements by Impact and Optical Disdrometers, Journal of Applied Meteorology, 40, 2083–2097, https://doi.org/10.1175/1520-0450(2001)040<2083:codsdm>2.0.co;2, 2001.

Ulbrich, C. W.: Natural Variations in the Analytical Form of the Raindrop Size Distribution, Journal of Climate and Applied Meteorology, 22, 1764–1775, https://doi.org/10.1175/1520-0450(1983)022<1764:nvitaf>2.0.co;2, 1983.

Ulbrich, C. W. and Lee, L. G.: Rainfall measurement error by WSR-88D radars due to variations in Z–R law parameters and the radar constant, Journal of Atmospheric and oceanic Technology, 16, 1017–1024, 1999.

Waterman, P.: Matrix formulation of electromagnetic scattering, Proceedings of the IEEE, 53, 805–812, https://doi.org/10.1109/proc.1965.4058, 1965.

Williams, C., Bringi, V., Carey, L., Chandrasekar, V., Gatlin, P., Haddad, Z., Meneghini, R., Munchak, s., Nesbitt, S., Petersen, W., Tanelli, S.,
Tokay, A., Wilson, A., and Wolff, D.: Describing the Shape of Raindrop Size Distributions Using Uncorrelated Raindrop Mass Spectrum Parameters, Journal of Applied Meteorology and Climatology, 53, 1282–1296, https://doi.org/10.1175/JAMC-D-13-076.1, 2014.

Zhang, G., Vivekanandan, J., and Brandes, E.: A method for estimating rain rate and drop size distribution from polarimetric radar measure-
ments, IEEE Transactions on Geoscience and Remote Sensing, 39, 830–841, https://doi.org/10.1109/36.917906, 2001.

Radars		
	RCWF	RCMD
Model	WSR-88D	Meteor 1700C
Peak Power	700 KW	250 KW
Operating Band	S-Band	C-Band
Wavelength	10.5 cm	5.3 cm
Longitude	~~121.7813~~121.78° ~~N~~ E	~~121.7728~~121.78° E
Latitude	~~25.0714~~25.07° N	~~25.0728~~25.07° ~~E~~N
Beamwidth	0.93°	0.90°
Range Resolution	250 m	100 to 500 m
Minimum System PhiDP	60°	10°
PRF	320-1300 Hz	250-2000 Hz
VCP	221	82

Table 1. Technical specifications of two polarimetric radars (RCWF and RCMD) used in the current work.

Location/Station	Latitude	Longitude	Height (m)	Range (km)
RCWF/RCMD	25.07	121.78	743	N/A
466930	25.17	121.54	659	26.8
466920	25.04	121.51	8	27.9
466910	25.19	121.52	765	29.2
466880	25.00	121.43	15	35.9
466950	25.63	122.07	5	68.6

Table 2. Equipment Location and height above mean sea level. Range is calculated as the haversine distance.

PARSIVEL Disdrometer	
Manufacturer	OTT HydroMet
Sampling Area	50 cm^2
Drop Size Range	0.06-24.5 mm
Velocity Range	0.05-20.8 m/s

Table 3. Disdrometer Characteristics

Figure 1. RCMD (C-Band) left and RCWF (S-Band) right at the Wufenshan weather station
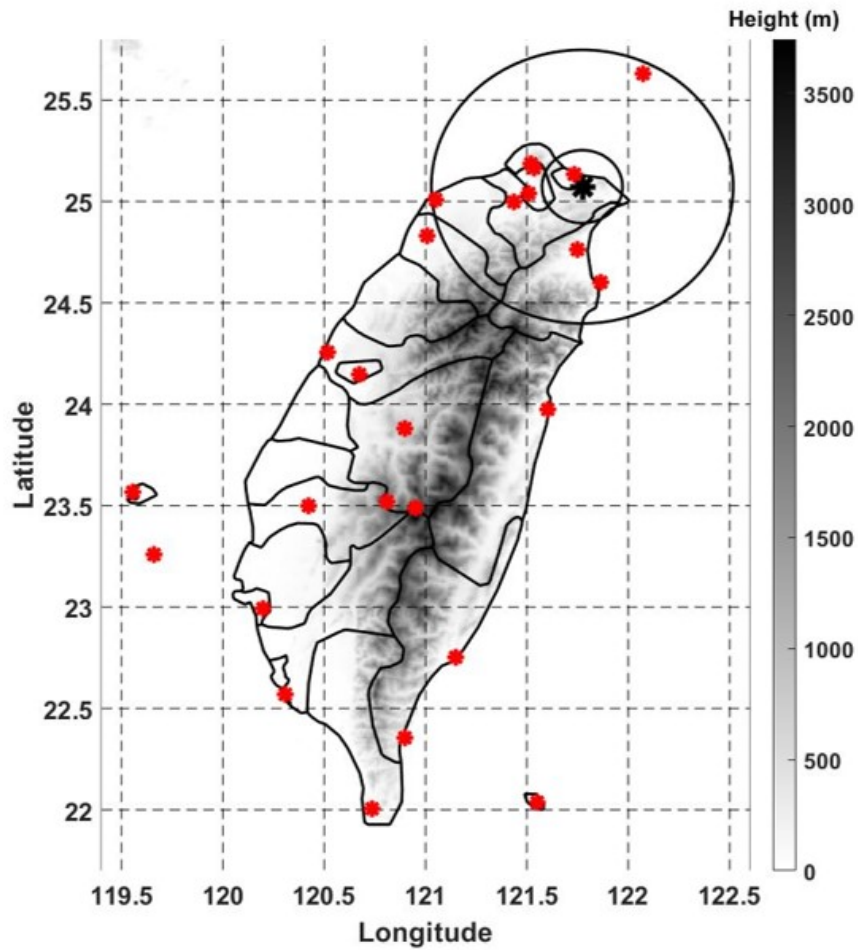
Figure 2. Taiwan - Instrument Locations. ~~The radar site is shown by the solid black asterisk on the North. Circles with~~ Radii (25 km and ~~100~~ 70 km~~radii~~) are drawn around the radar location~~to indicate the data viability region~~. Measurement stations with disdrometers are shown in red. Terrain height is indicated in grayscale throughout the map for reference.
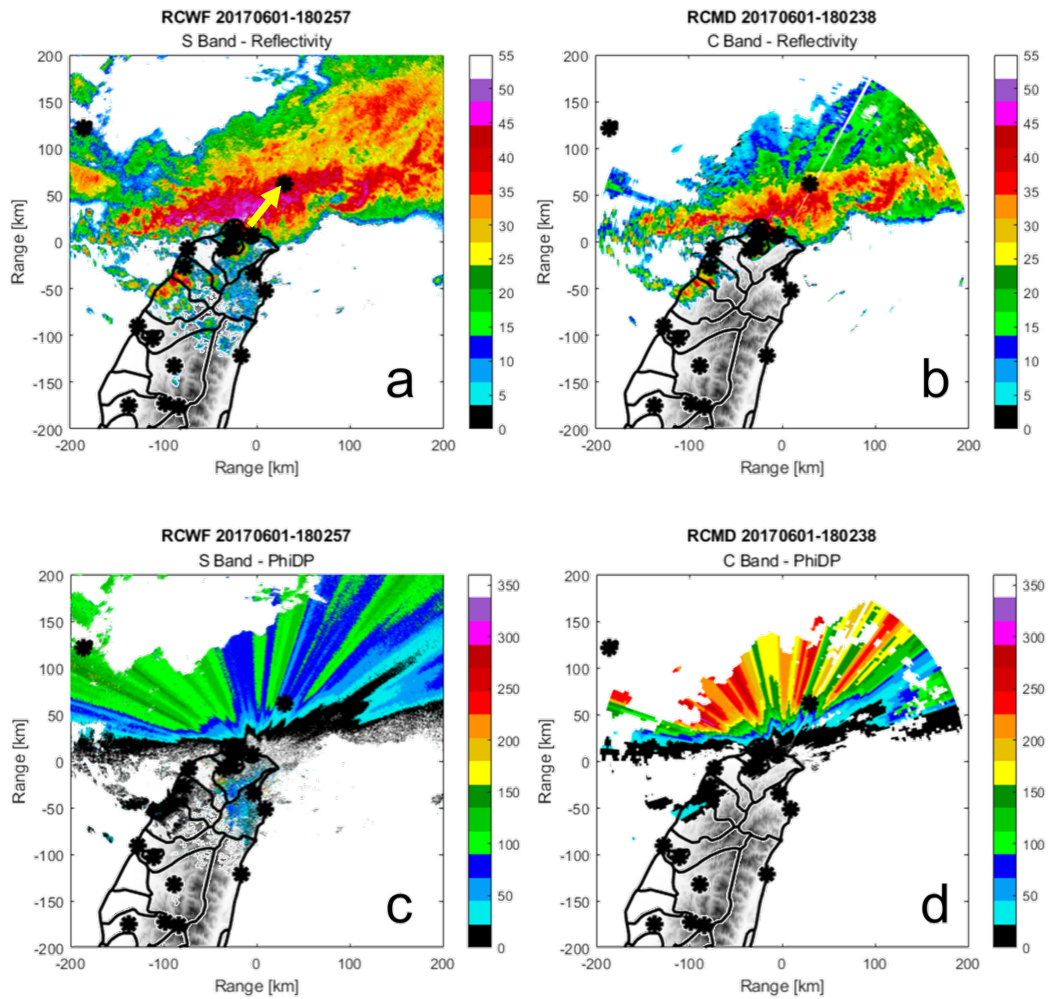
Figure 3. Panels a and b show the reflectivity measured in S-band and C-band, respectively. The yellow arrow in panel a indicates the radial path from the radars to the disdrometer location of interest. Panels c and d contain the raw differential phase measurements recorded in S-band and C-band.
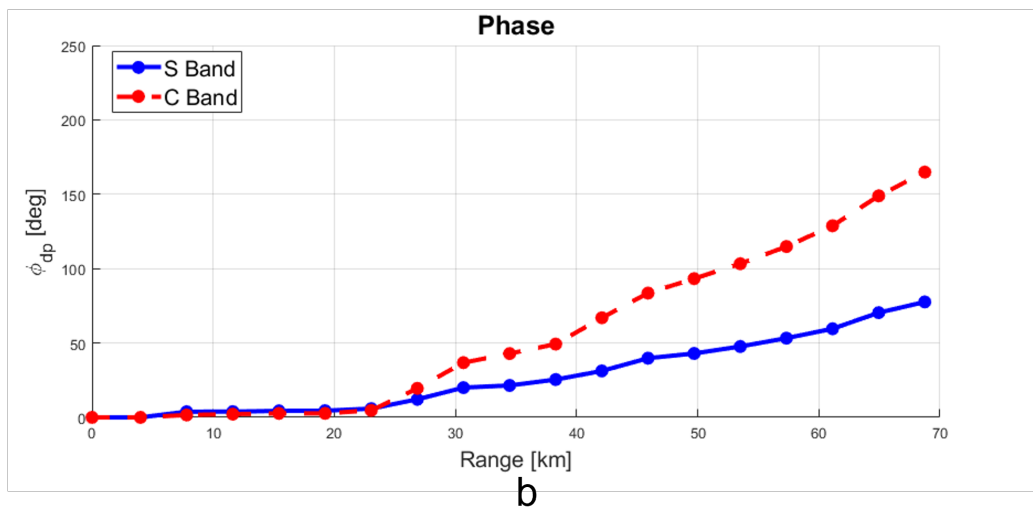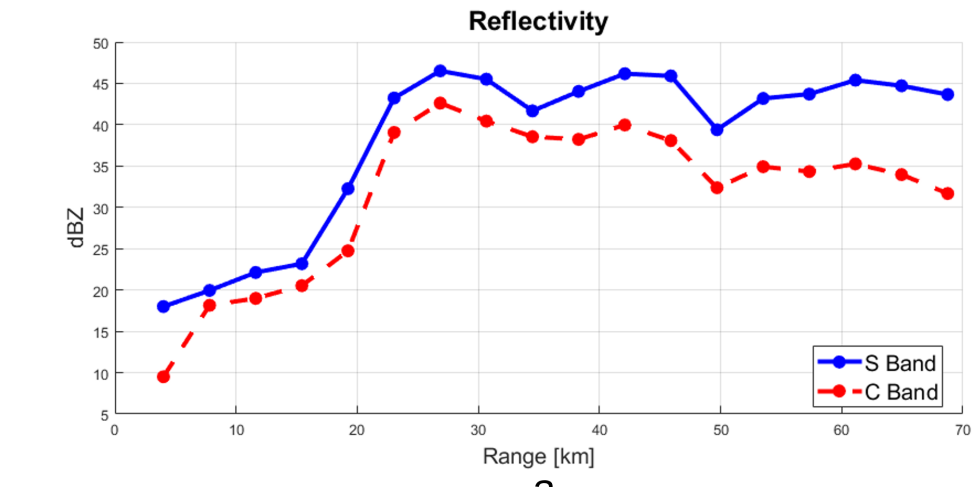
Figure 4. The data along the radial indicated in Figure 3 following preprocessing yields the reflectivity (a) and differential phase (b) used in the retrieval for this measurement time.
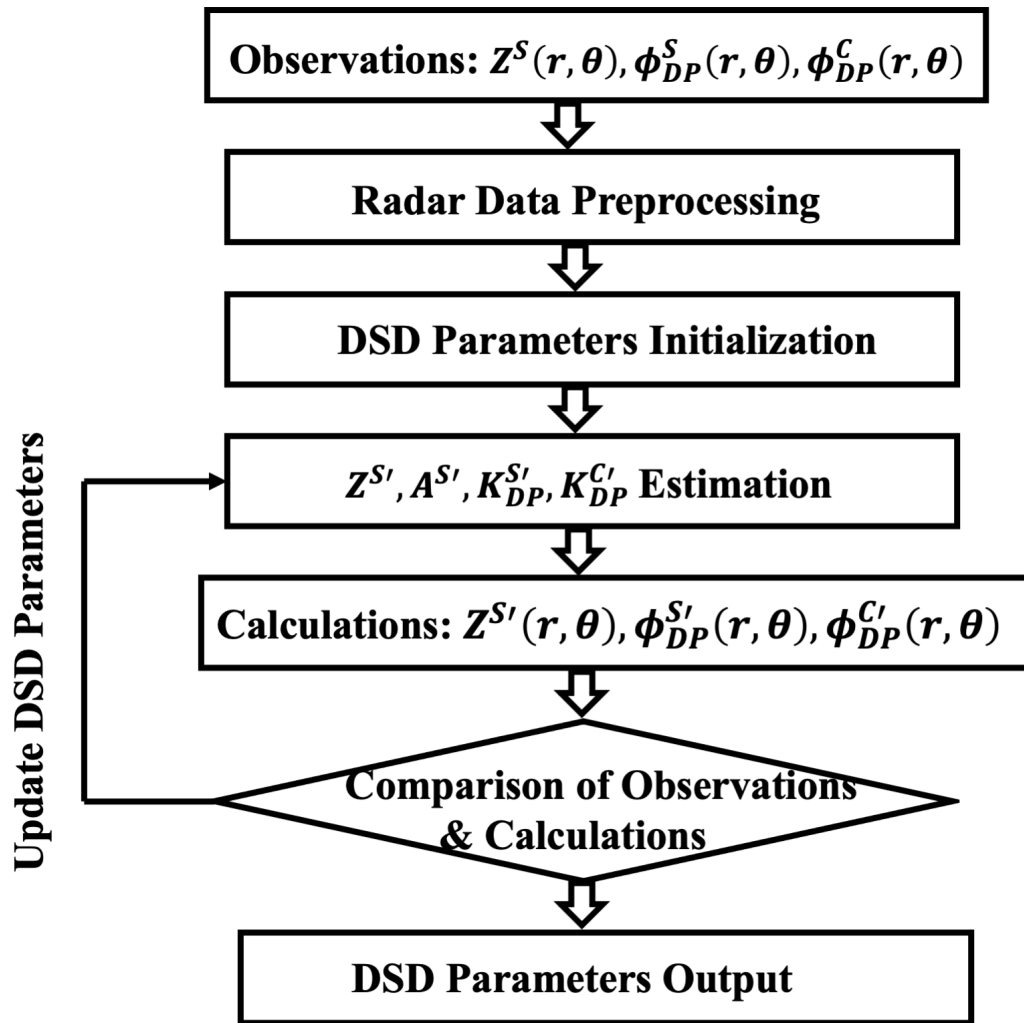
Figure 5. The algorithm applied to each gate seeks DSD parameters which produce reflectivity and estimated specific differential phase values that correspond to the radar reflectivity and differential phase values observed at the disdrometer location by RCMD and RCWF. The calculated values are indicated as $Z^{S'}$, $\phi_{DP}^{S'}$, etc. as opposed to the radar observed values indicated as Z^{S}, ϕ_{DP}^{S}, etc.
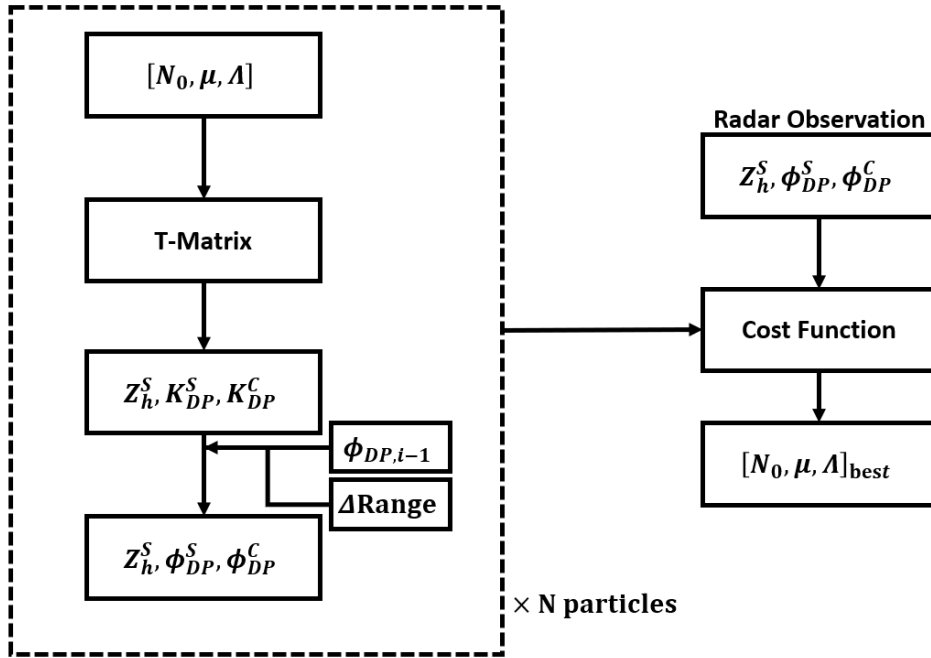
Figure 6. Particle Swarm Optimization for Gate of Interest. ~~Each~~ The left dashed box denotes the calculations for each particle which has an independent set of gamma distribution defining variables that is used to estimate reflectivity and specific differential phase values using the T-Matrix method. Range differentials and previously determined phase are used to produce estimated parameters which can then be applied to a cost function relative to the observed values.
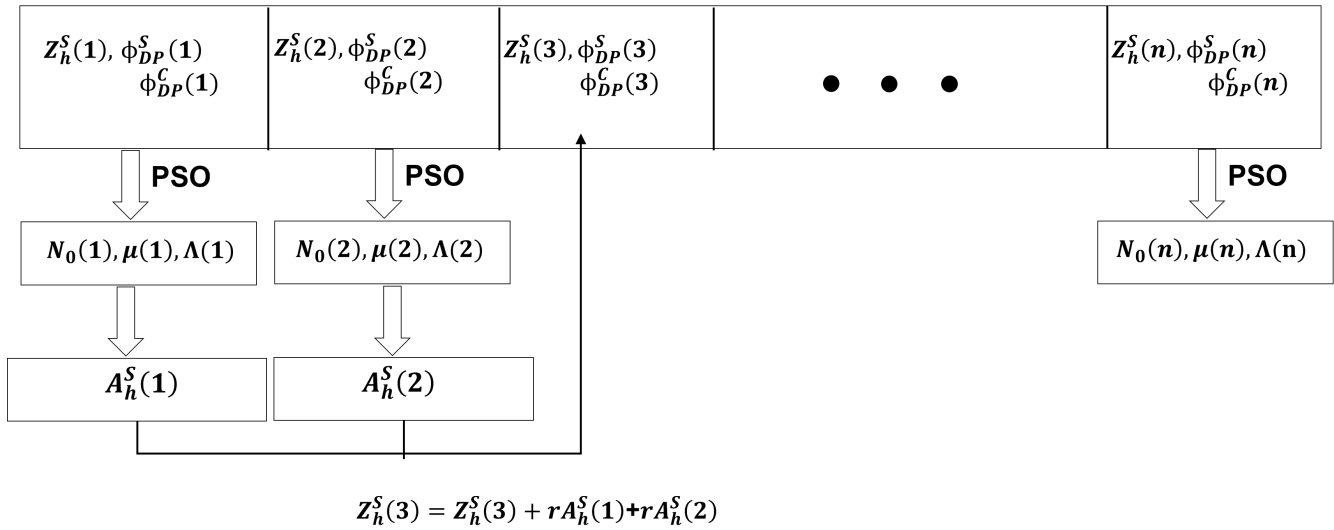
Figure 7. Retrieval Along Radial. The process begins with the first gate which is assumed to be unaffected by attenuation. The reflectivity and phase information serve as inputs to the PSO of each gate and produce DSD values that can be used to calculate the local attenuation. The next gate's observed reflectivity value is updated with any previously accumulated attenuation before being used in the next optimization. The process continues until the final gate's values are determined.
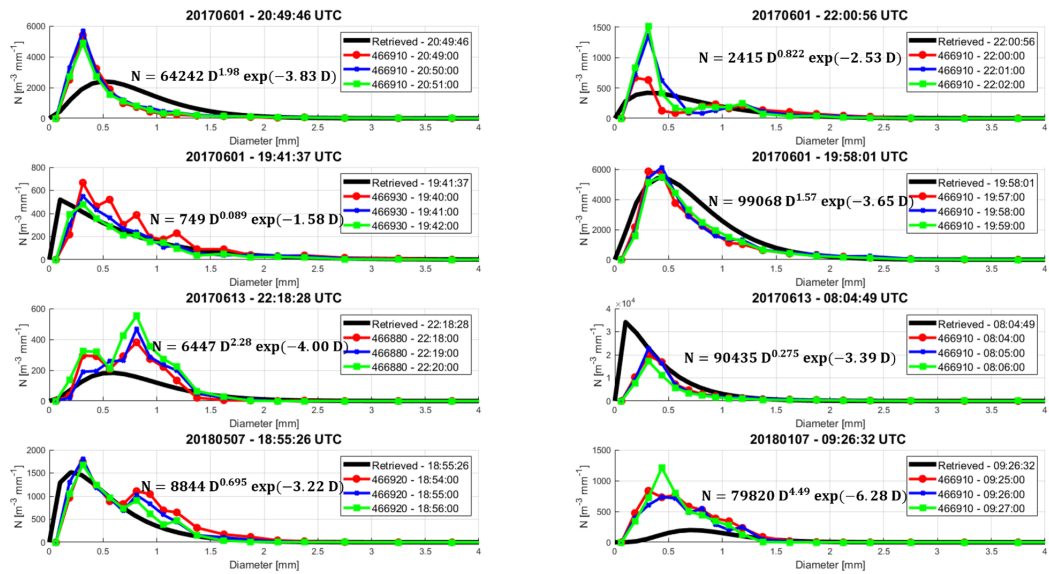
Figure 8. ~~Panels a-d show four qualitative examples of the results achieved by the algorithm. Local disdrometer particle size concentrations are~~ The retrieved DSD is shown ~~by the red markers of~~ in black on each plot ~~while the algorithm~~ with it's ~~retrieval results are~~ gamma distribution equation. The DSD of the closest disdrometer record is plotted ~~with a black dashed line~~ in blue while the time previous and next record time are shown in red and green, respectively.
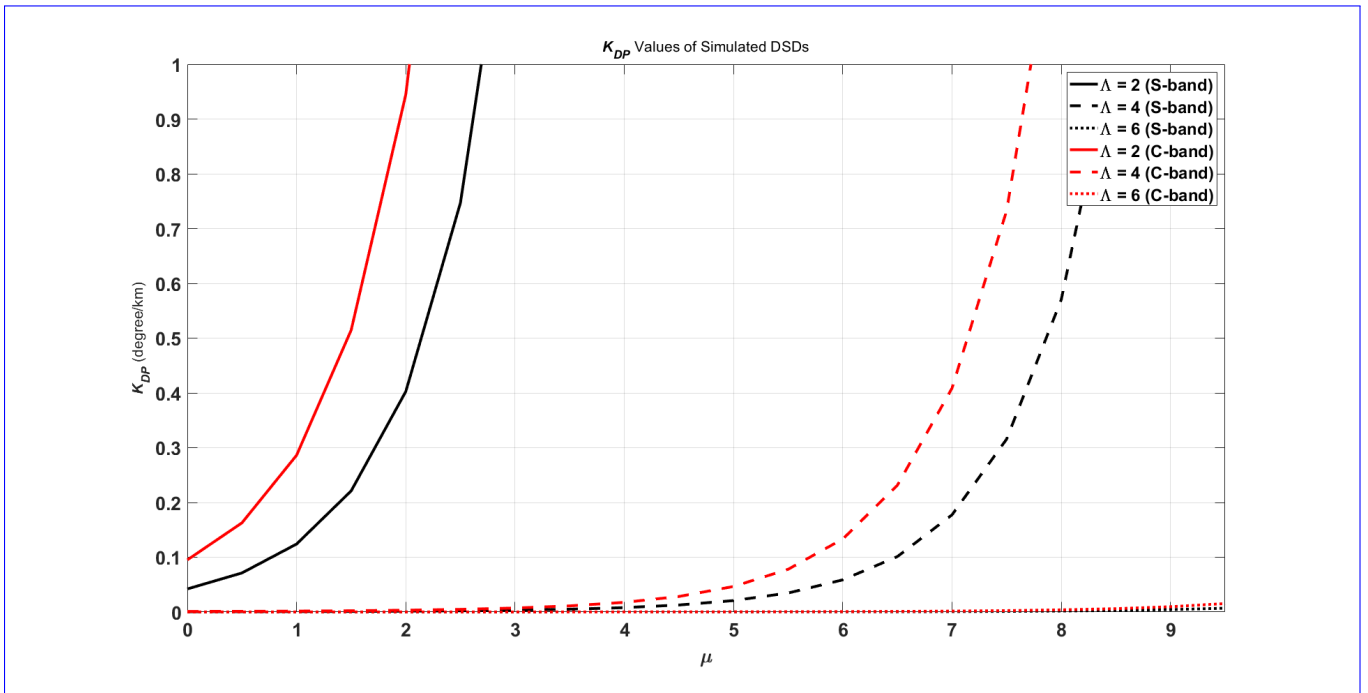
Figure 9. K_{DP} is simulated for DSDs of varying μ and Λ values with fixed $N_0 = 8000$. A sepation between the K_{DP} values is clear at the two radar bands except for large values of Λ.
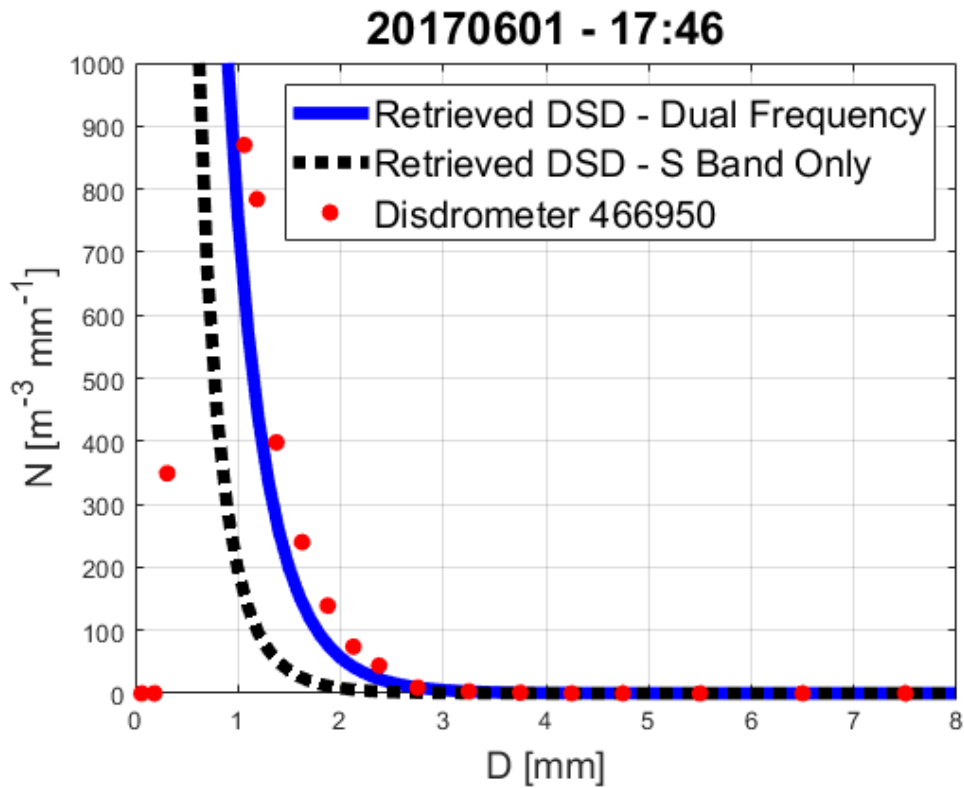
Figure 10. This example demonstrates the dual polarization/dual frequency approach represented by the solid blue line much more closely matches the disdrometer measurements shown with red markers. The black dashed line was produced by only using the dual polarization data from RCWF.
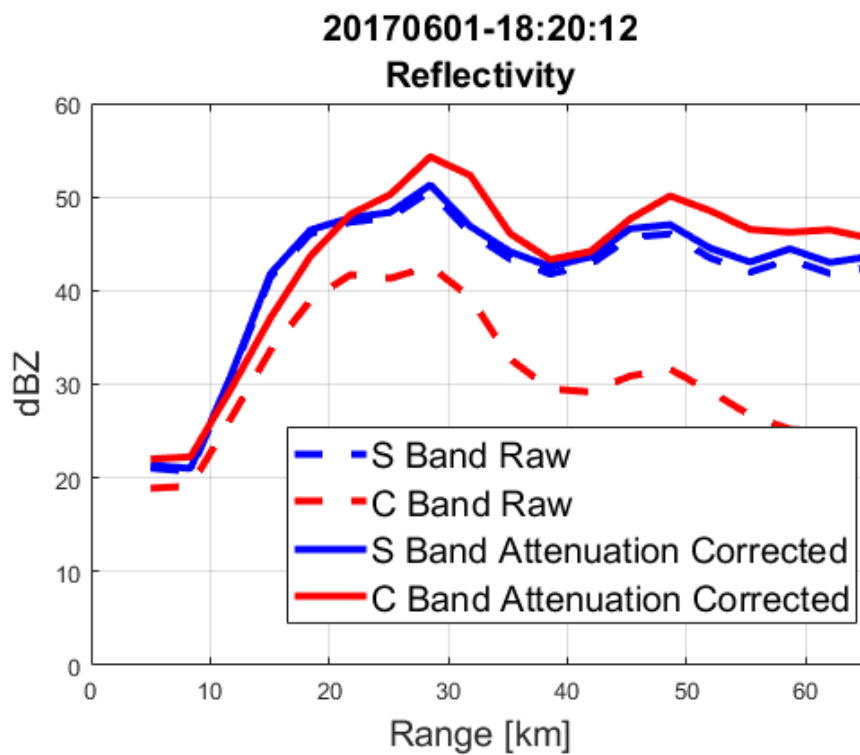
Figure 11. The S-band reflectivity is relatively unaffected by attenuation as presented by the raw reflectivity values shown with a dashed blue line and the attenuation-corrected reflectivity values indicated by solid blue. The corrected C-band reflectivities shown with red solid line match very well with the S-band values.
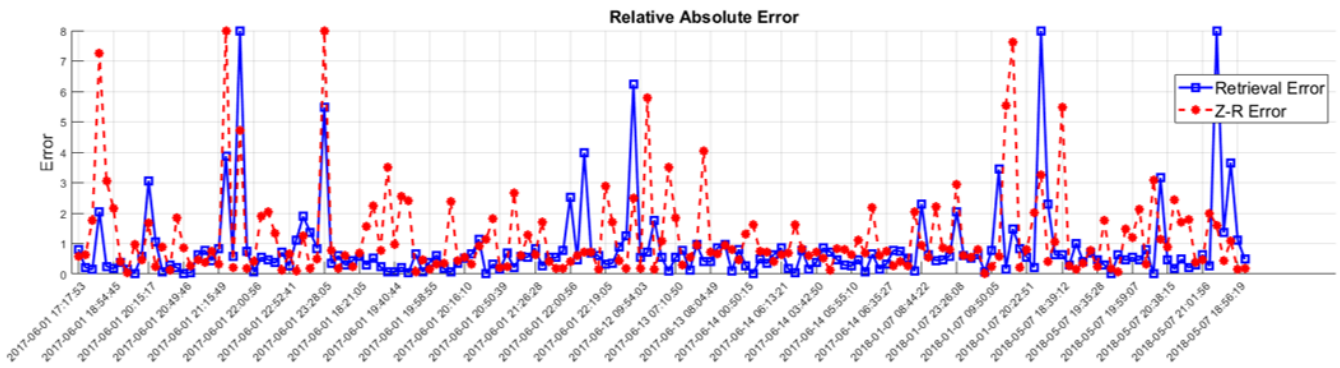
Figure 12. Relative Absolute Error (RAE) of the retrieval results are shown in blue while the *Z-R* method's RAE is shown in red. Five outlier values are truncated at the vertical limit of the plot in order to preserve the relative scale.